Supporting Information

Usluer et al. 10.1073/pnas.1715836115

SI Methods

Sequence Comparison. The sequence for AlfA was subjected to a BLAST search (1), yielding only three matches of significant homology. These three matches were subjected to BLAST, increasing the size of the pool of AlfA homologs missing subdomain IIb, and this processes was repeated until no new homologs with the AlfA domain architecture were found. Multiple sequence alignment were calculated with MAFFT (2), using AlfA and the pool of close homologs and large representative samples of other bacterial actin familes (MamK, MreB, ParM, Alp12, Alp7).

AlfA Expression Constructs. Previously described untagged expression constructs using a codon-optimized *alfa* gene were used to express wild-type (pJKP100) and nonbundling (pJKP102) AlfA (3, 4). AlfA-F12A was generated by site-directed mutagenesis of pJKP100. For nonassembling mutants the AlfA coding region was cloned into pSMT3-Kan (5), which inserted a His-SMT3/SUMO tag at the N terminus of AlfA. The tag can be cleaved by ULP1 protease, leaving only two residual nonnative residues at the N terminus.

Protein Expression and Purification. Recombinant AlfA constructs were expressed from isfopropyl-β-D-thiogalactopyranoside (IPTG) -inducible promoters in *Escherichia coli* C43 cells at 18 °C overnight, as previously described (3). Wild-type, nonbundling AlfA, and AlfA-F12A were purified using a protocol similar to previous studies (3, 4), using cycling between polymerized and unpolymerized states as an initial bulk purification step. Cell pellets were resuspended in lysis buffer (25 mM Tris pH 7.5, 300 mM KCl), lysed by sonication, and the lysate cleared by ultracentrifugation for 1 h at 4 °C at $105,000 \times g$ in a type 50.2 Ti rotor (Beckman Coulter). AlfA was polymerized in the cleared lysate by addition of 5 mM ATP and 12 mM $MgCl_2$ on ice for 30 min, and then pelleted by ultracentrifugation for 1 h. The supernatant was discarded, and pelleted filaments were resuspended in depolymerization buffer (25 mM Tris pH 7.5, 300 mM KCl, 5 mM EDTA) then dialyzed overnight against the same buffer. Unpolymerized material was removed by ultracentrifugation, and the polymerization-depolymerization cycle was repeated. The final soluble AlfA sample was then applied to a Superdex 200 size-exclusion column in polymerization buffer, peak fractions were pooled and concentrated to 100–200 μM, then flash-frozen in liquid nitrogen and stored at −80 °C or stored for up to a week at 4 °C.

Cycling between polymerized and unpolymerized states could not be used to purify mutants designed to interfere with assembly. Instead, these were purified by Ni-NTA affinity chromatography, the His-SMT3/SUMO tag removed by cleavage with ULP1, followed size-exclusion chromatography on a Superdex 200 column in polymerization buffer. Polymerization of wild-type AlfA purified in the same way from the same expression vector was indistinguishable from polymerization of untagged wild-type AlfA.

Negative-Stain Electron Microscopy. Wild-type and mutant AlfA samples were polymerized for 15 min at room temperature in polymerization buffer plus 1 mM nucleotide and 1 mM $MgCl_2$. Samples were applied to glow-discharged 400-mesh carbon-coated grids, and negatively stained with 0.7% uranyl formate (6). Images were obtained on an FEI Morgagni microscope operating at 100 kV, at 22,000× magnification, recorded on an Orious CCD camera (Gatan). For quantification of assembly of wild-type and F12A mutants images were collected on an FEI Spirit microscope operating at 120 kV with an Ultrascan 4k × 4k CCD camera (Gatan). We used Leginon for automated data collection, acquiring images at random positions using the raster function for high magnification targeting (7).

Cryo-EM Data Acquisition. Nonbundling AlfA was assembled at room temperature, at 5 μM AlfA in polymerization buffer with 5 mM AMPPNP and 5 mM $MgCl_2$ added. Samples were applied to glow-discharged C-FLAT 1.2/1.3–4C holey carbon grids (Protochips) and plunge-frozen in liquid ethane in a Vitrobot Mark IV vitrification device (FEI). Data were collected with an FEI Titan Krios microscope operated at 300 kV on a K2 Summit direct electron detector (Gatan) in operating in superresolution mode with a pixel size of 0.5 Å per pixel. Movies were recorded for 7.2 s, with 0.2-s frames, 72 e⁻/Å² total dose per movie. Leginon was used for automated data acquisition (7).

Cryo-EM Image Processing. Movies were aligned, dose-weighted, and Fourier-binned using MotionCor2 (8). Defocus parameters were determined from the unweighted aligned sums using GCTF (9). Filaments were automatically identified using RELION (10), and extracted in overlapping 448-Å boxes using a step size of 25 Å to match the AlfA helical rise. This yielded 123,296 boxed segments. Helical segments were subjected to reference-free 2D classification in RELION, and poorly aligning segments were rejected from further processing, leaving a dataset of 113,222 segments for 3D processing.

An initial reconstruction was calculated using iterative helical real-space reconstruction in SPIDER, essentially as described previously (11–13). This model was low-pass–filtered at 60 Å and used as an initial model for helical refinement in RELION (10, 14, 15). After initial gold-standard helical refinement using a spherical mask yielded a structure at about 5-Å resolution, helical segments were subjected to the RELION particle polishing routine, and refinement was continued using a shape-based soft-edged mask enclosing ~six AlfA protomers (Fig. S4*B*). The final reported resolution is from a Fourier shell correlation (FSC) curve corrected for masking artifacts.

Atomic Model Building and Analysis. An initial structure of the AlfA protomer was generated asymmetrically using RosettaCM (16) for comparative modeling into the EM density map, using a diverse set of actin atomic structures as templates (PDB ID codes: 1JCE, 2FSJ, 2ZGY, 3I33, 3JS6, 4APW, 4B1Y, 4KBO, 4PL7, 4RTF, 4XE7, 4XHP, 5EC0, 5F0X, 5LJW). Several loop regions (residues 65–83, 36–44, 195–215) were then rebuilt in Rosetta in the context of the helical lattice. This was followed by automated refinement of the entire structure in Rosetta using helical symmetry constraints using the protocol described by Wang et al. (17). Finally, some side-chain rotamers were adjusted manually to improve fit to density.

The sizes of interacting surfaces between domains in AlfA and other actin filaments were calculated using the PDBePISA server (18). All cryo-EM structures and atomic models were visualized and figures prepared in Chimera (19).

1. Boratyn GM, et al. (2013) BLAST: A more efficient report with usability improvements. *Nucleic Acids Res* 41:W29–W33.

2. Katoh K, Misawa K, Kuma K, Miyata T (2002) MAFFT: A novel method for rapid multiple sequence alignment based on fast Fourier transform. *Nucleic Acids Res* 30:3059–3066.

3. Polka JK, Kollman JM, Agard DA, Mullins RD (2009) The structure and assembly dynamics of plasmid actin AlfA imply a novel mechanism of DNA segregation. *J Bacteriol* 191:6219–6230.

4. Polka JK, Kollman JM, Mullins RD (2014) Accessory factors promote AlfA-dependent plasmid segregation by regulating filament nucleation, disassembly, and bundling. *Proc Natl Acad Sci USA* 111:2176–2181.

5. Mossessova E, Lima CD (2000) Ulp1-SUMO crystal structure and genetic analysis reveal conserved interactions and a regulatory element essential for cell growth in yeast. *Mol Cell* 5:865–876.

6. Ohi M, Li Y, Cheng Y, Walz T (2004) Negative staining and image classification—Powerful tools in modern electron microscopy. *Biol Proced Online* 6:23–34.

7. Suloway C, et al. (2005) Automated molecular microscopy: The new Leginon system. *J Struct Biol* 151:41–60.

8. Zheng SQ, et al. (2017) MotionCor2: Anisotropic correction of beam-induced motion for improved cryo-electron microscopy. *Nat Methods* 14:331–332.

9. Zhang K (2016) Gctf: Real-time CTF determination and correction. *J Struct Biol* 193:1–12.

10. He S, Scheres SHW (2017) Helical reconstruction in RELION. *J Struct Biol* 198:163–176.

11. Egelman EH (2010) Reconstruction of helical filaments and tubes. *Methods Enzymol* 482:167–183.

12. Bergeron JR, et al. (2017) Structure of the magnetosome-associated actin-like MamK filament at subnanometer resolution. *Protein Sci* 26:93–102.

13. Sachse C, et al. (2007) High-resolution electron microscopy of helical specimens: A fresh look at tobacco mosaic virus. *J Mol Biol* 371:812–835.

14. Kimanius D, Forsberg BO, Scheres SH, Lindahl E (2016) Accelerated cryo-EM structure determination with parallelisation using GPUs in RELION-2. *eLife* 5:e18722.

15. Scheres SH (2012) RELION: Implementation of a Bayesian approach to cryo-EM structure determination. *J Struct Biol* 180:519–530.

16. Song Y, et al. (2013) High-resolution comparative modeling with RosettaCM. *Structure* 21:1735–1742.

17. Wang RY, et al. (2016) Automated structure refinement of macromolecular assemblies from cryo-EM maps using Rosetta. *eLife* 5:e17219.

18. Krissinel E, Henrick K (2007) Inference of macromolecular assemblies from crystalline state. *J Mol Biol* 372:774–797.

19. Goddard TD, Huang CC, Ferrin TE (2007) Visualizing density maps with UCSF Chimera. *J Struct Biol* 157:281–287.
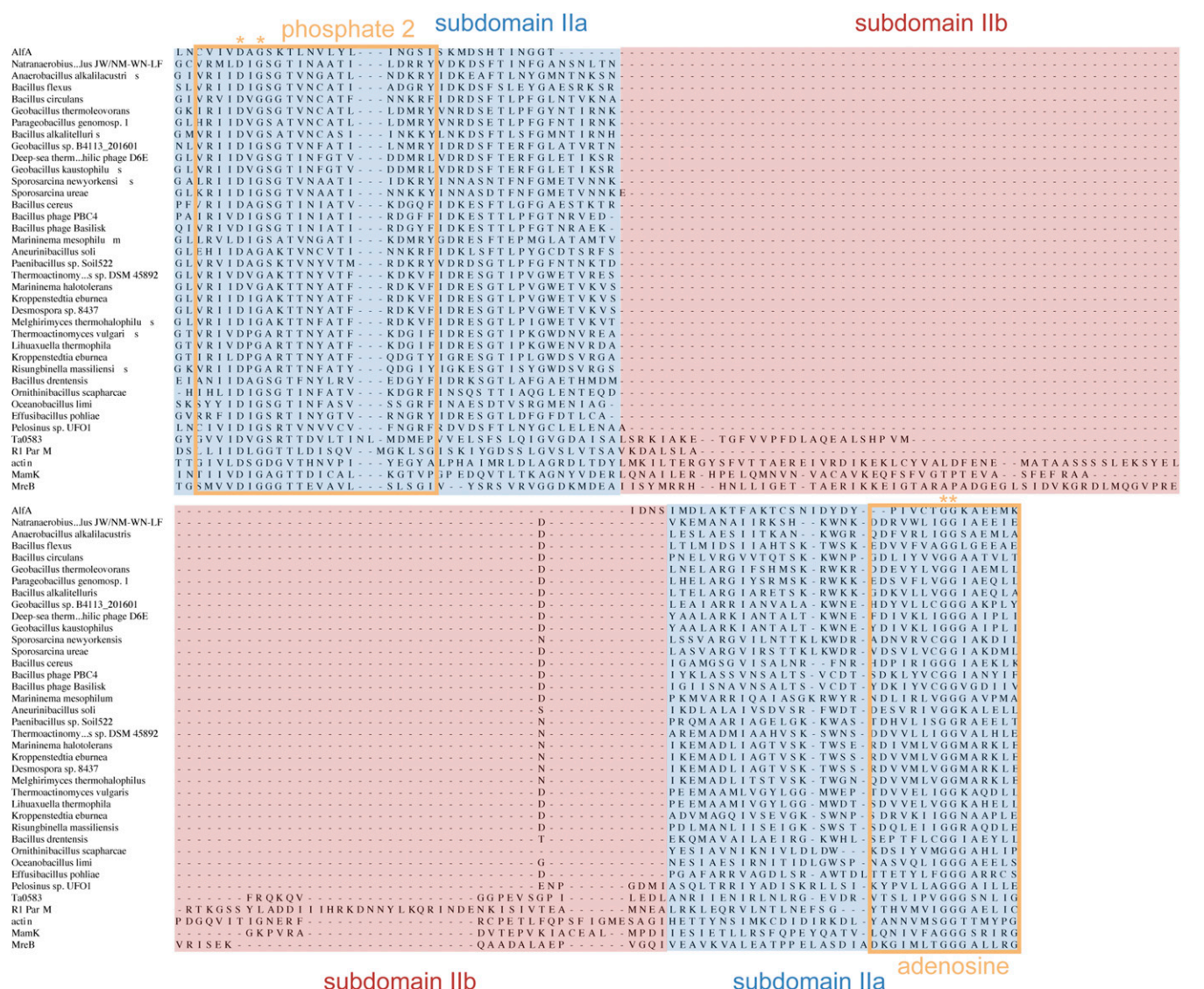
Fig. S1. Sequence alignments of domain II. Multiple sequence alignment of subdomain IIb (red) and flanking regions in subdomain IIa (blue), demonstrates a family of bacterial and phage actins that lack subdomain IIb. The conserved phosphate 2 and adenosine motifs are outlined in orange and universally conserved residues highlighted with asterisks. The overall sequence identity between AlfA and other actins missing subdomain IIb is ~20%, while the identity to other bacterial actins is between 11% and 15%.

Fig. S2. Conformational differences between free and filament-bound actins. Four different actins are show in their free conformations from crystal structures (gray) and filament-bound conformations from high-resolution cryo-EM reconstructions (color). In each case the major conformational change is a rotation of domains I and II relative to each other, yielding a flatter protomer in the filament. Arrows indicate the direction of the conformational change. The structure pairs were aligned on domain Ia in each case. PDB ID codes are indicated for both states.

Fig. S3. Optimization of AlfA cryo-EM samples. (*A*) Cryo-EM image of AlfA at 100 mM KCl, where single filaments laterally associate into bundles with irregular thickness. (*B*) Cryo-EM image of AlfA at 1 M KCl, where bundle formation is inhibited but increased solvent density reduces contrast with the filaments. (*C*) Reconstruction at 12-Å resolution of AlfA filaments in 1 M KCl. (*D*) Cryo-EM image of AlfA with four surface lysines (K21, K22, K101, K102) mutated to alanine (the "quad" mutant), which inhibits bundling at low salt concentration. Images in *B* and *D* are both at −1.5-µm defocus.
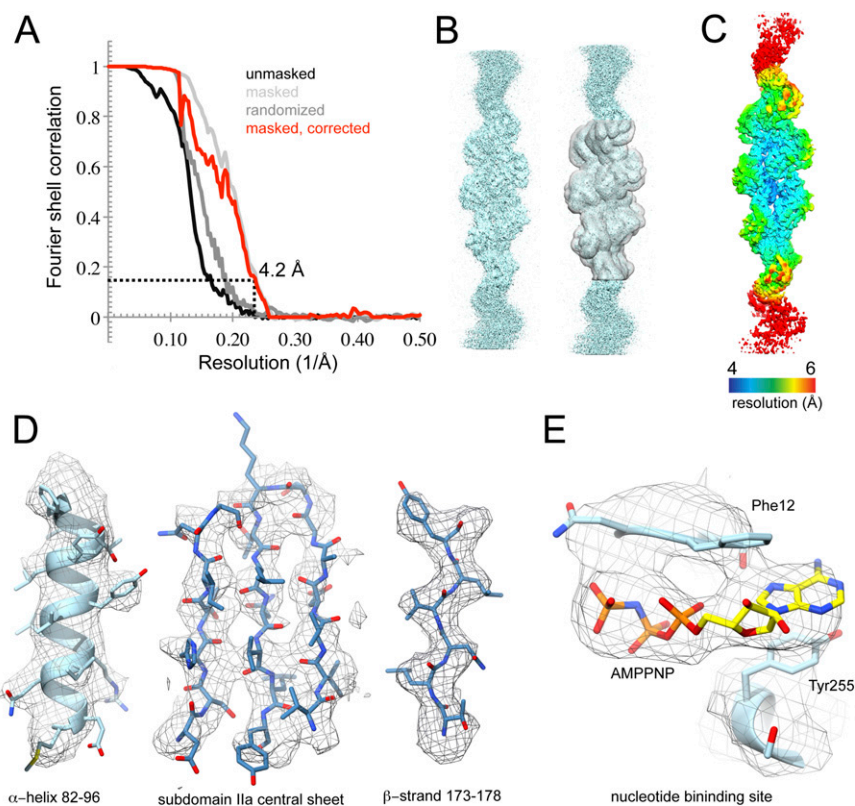
Fig. S4. Cryo-EM reconstruction of AlfA. (*A*) FSC curves for final AlfA reconstruction. The final resolution calculated from the masked filament and corrected for masking effects is 4.2 Å. (*B*) One unfiltered half map from the final reconstruction, shown with the mask used for calculating the FSC curves in *A* (*Right*). (*C*) Local resolution estimate calculated in RELION. (*D*) Regions of representative density in the structure. (*E*) Cryo-EM density in the nucleotide binding site.
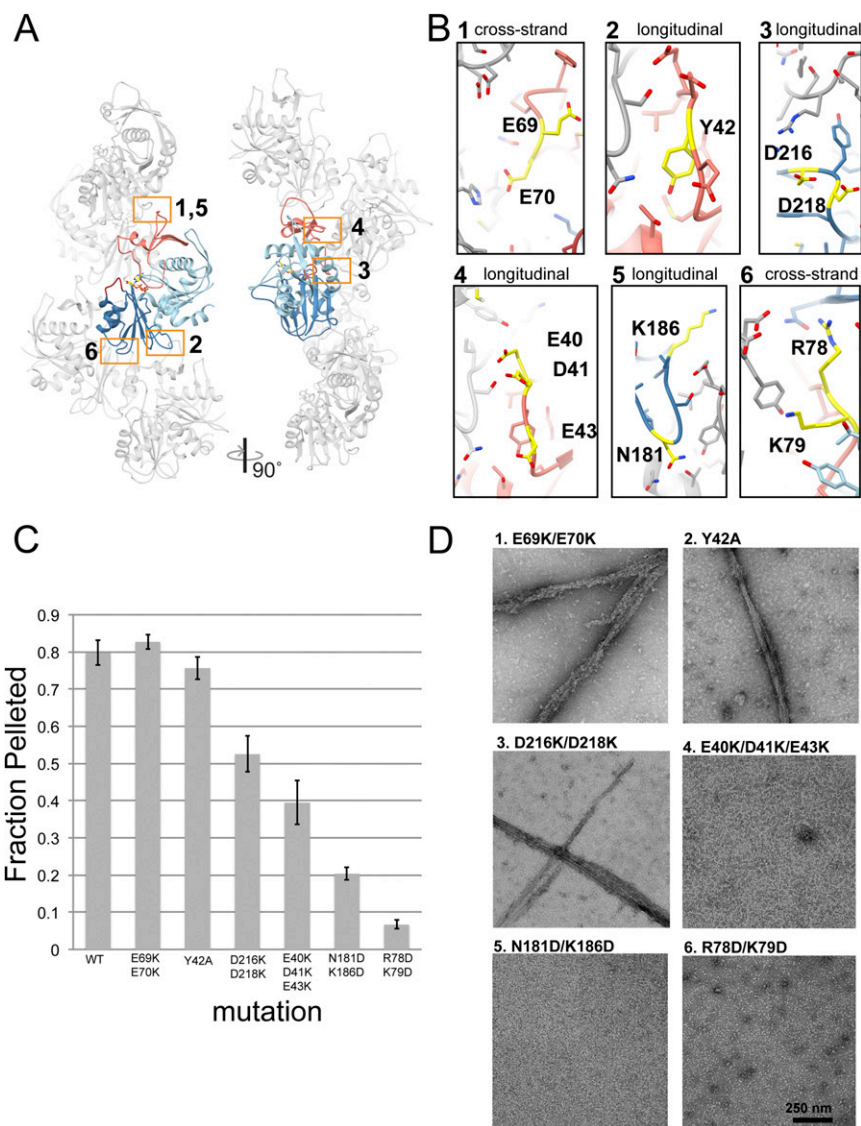
Fig. S5. Comparison of AlfA ATP binding with other actin homologs. In each panel the AlfA ATP-binding site is superimposed on the binding site of an actin homolog. The coloring is as in Fig. 3, with the AlfA ATP in yellow and the homolog ATP in gray.

Fig. S6. Analysis of AlfA-F12A assembly in the presence of ATP and ADP. Representative low-magnification (4,400×) and high-magnification (67,000×) images of negatively stained wild-type and F12A AlfA. For each condition a set of randomly targeted high-magnification images was acquired, and high-magnification images were scored as either having AlfA polymer or not, as quantified in Table S2.

Fig. S7. Evolutionary variation in the contribution of different subdomains to actin assembly interfaces. (*A*) For each actin the area of interaction surfaces for each subdomain is plotted, showing contributions to longitudinal (vertical lines) and cross-strand (horizontal lines) interfaces. Scale bar at the *Bottom Left* indicates size of interfaces in Å². (*B*) The relative size of assembly interfaces for each subdomain are plotted as a fraction of total protomer surface area.

Fig. S8. AlfA assembly mutants. Six assembly mutants were designed on the basis of and AlfA homology model fit into a preliminary 12-Å reconstruction of the AlfA filament. (*A*) Atomic model of the AlfA filament with a single protomer colored as in Fig. 1, with locations of designed assembly mutants indicated by orange boxes. (*B*) Close-up views of the different designed mutations (yellow) in the final refined structure. (*C*) Quantification of mutant polymerization by filament pelleting assay. The fraction of each mutant pelleted by ultracentrifugation is plotted for each mutant (*n* = 5, error bars represent SEM). The severity of polymerization defects appears to correlate with the position of the residue with respect to the interface in the final structure. For example, while Tyr42 is close to the longitudinal interface, its side-chain is pointed away from the neighboring protomer in the final model and so its mutation to alanine has a negligible effect on polymerization. On the other hand, the side-chain of Lys79 is pointed directly across the interface at the neighboring protomer, explaining why mutation at this site severely inhibits polymerization. (*D*) Representative negative-stain images of AlfA designed assembly mutants.

Table S1. Cryo-EM data collection and refinement statistics

| Data collection and refinement	Statistics
Data collection	
Microscope	Titan Krios
Voltage, kV	300
Detector	K2 summit, superresolution
Electron exposure, $e^-/Å^2$	72
Frames per exposure	36
Pixel size, Å	0.5
Defocus range, μm	0.7–2.5
Reconstruction	
Refined helical rotation, °	157.7
Refined helical rise, Å	24.4
Helical segments	113,222
Resolution (0.143 FSC), Å	4.2
Model composition	
Protein residues	275
Ligands	1 (AMPPNP)
Model statistics	
Clash score	7.77
Molprobity score	2.1
Ramachandran favored, %	84
Ramachandran outliers, %	6
Structure deposition	
EMDB ID (cryo-EM map)	EMD-7134
PDB ID (atomic model)	6BQW

Table S2. Fraction of micrographs containing polymer under different nucleotide conditions

| AlfA, μM	Nucleotide	Wild-type (n)	F12A (n)
1.5	ATP	0.34 (245)	0 (109)
4.5	ATP	0.97 (74)	0.10 (231)
10	ADP	0.20 (97)	0 (225)
30	ADP	0.56 (160)	0 (131)
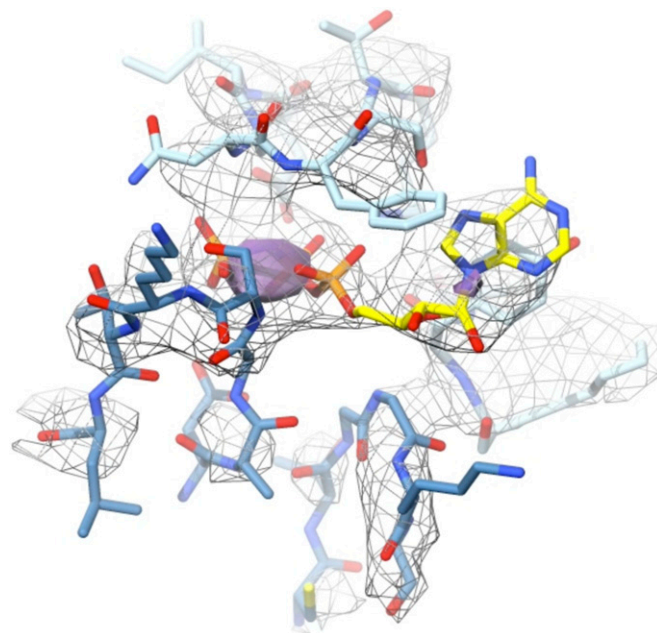
Movie S1. The AlfA ATP binding site. First revolution: Residues surrounding the AlfA ATP binding site are shown fit in the cryo-EM density (mesh). ATP is shown in yellow and residues in subdomain Ia in light blue and IIa in dark blue. At higher contour levels (transparent purple) it is clear that the region around the β- and γ-phosphates of ATP have the highest density. Second revolution: The AlfA backbone is rendered as a ribbon, and the binding site of ParM (PDB ID code 5AEY) is overlain in dark gray to highlight the distinct difference in positioning of the adenosine base.

Movie S1
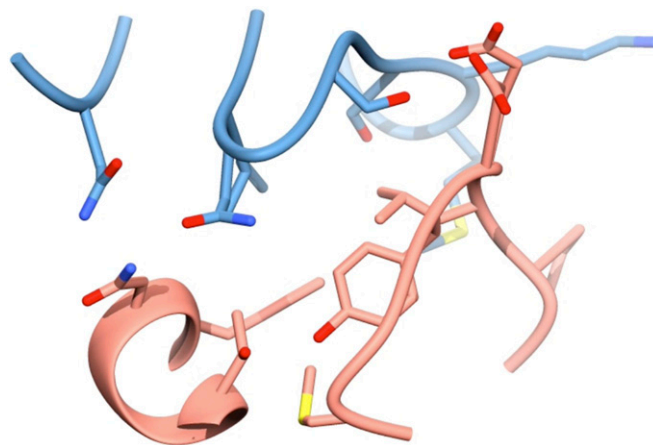
Movie S2. AlfA filament longitudinal contacts. The longitudinal interface between subdomain Ib (residues 37–45 and 59–65, in pink) and subdomain IIa (residues 162–164 and 179–188, in blue).

Movie S2
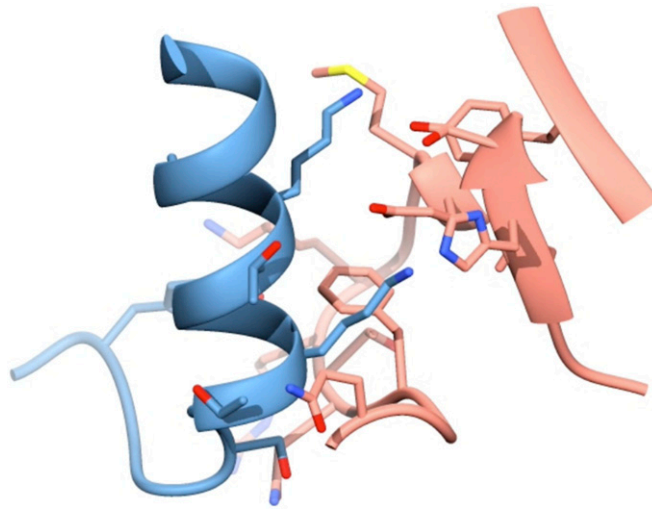
Movie S3. AlfA filament lateral contacts. The longitudinal interface between subdomain Ib (residues 69–82, 35–39, and 54–56 in pink) and subdomain IIa (residues 201–218, in blue).

[Movie S3](#)